ACS OMEGA

Open Access

http://pubs.acs.org/journal/acsodf

Article

Lithium Storage Behavior of Expanded Microcrystalline Graphite/Fe_2O_3 Anode for Lithium-Ion Batteries

Sen Yang,* Ning Zhao, Kang Zheng, Lu Sun, and Jiahui Niu

Cite This: *ACS Omega* 2025, 10, 17673−17683

Read Online

ACCESS | Metrics & More | Article Recommendations | Supporting Information

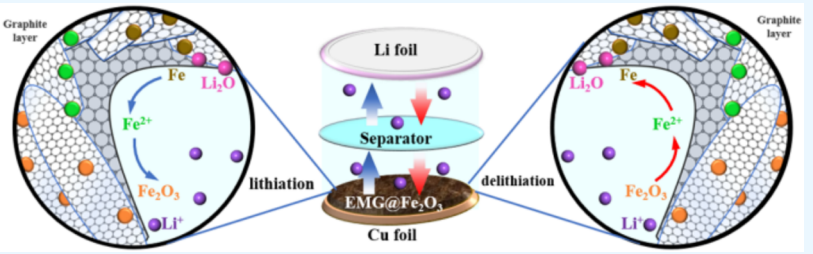

ABSTRACT: Driven by the pressing need for improved performance of lithium-ion batteries in electric vehicles and portable electronics, this research aims to develop novel high-performance anode materials. Innovatively, expanded microcrystalline graphite (EMG) is used as the matrix material. Through a simple synthesis strategy, Fe_2O_3 nanoparticles are successfully introduced to prepare expanded microcrystalline EMG/Fe_2O_3 composites. The study systematically investigates the effects of different doping ratios on the electrochemical performance of the materials. The experimental results demonstrate that the EMG/Fe_2O_3-2 composite material exhibits the most excellent lithium storage performance: the initial discharge specific capacity is 1114.10 mAh·g^{-1}, and after 100 cycles, the discharge specific capacity remains at 1007.05 mAh·g^{-1}, with a capacity retention rate as high as 90.39%. The outstanding electrochemical performance is mainly attributed to the following factors. On the one hand, the porous structure of EMG not only provides an effective buffering space for the volume expansion of Fe_2O_3, but its complex conductive network also significantly enhances the charge transport efficiency of the composite material. On the other hand, the high theoretical specific capacity of Fe_2O_3 nanoparticles, combined with the EMG matrix, forms a synergistic effect that enhances the specific capacity of the composite material. This thesis not only elucidates the synergistic mechanism between EMG and Fe_2O_3 but also provides new strategies and perspectives for the performance breakthrough of lithium-ion battery anode materials.

1. INTRODUCTION

With the development of environmentally friendly economies, the global demand for green and recyclable energy solutions has been rapidly increasing.[1] Lithium-ion batteries have the advantages of high-power density, good environmental friendliness and lengthy cycle life. They have been widely used in energy storage devices, transportation and smart grid energy storage and are showing a booming trend in the electric vehicle industry. In order to meet the demand for high-capacity and long-life lithium-ion batteries, researchers have extensively explored the development of new electrode materials in recent years.[2,3] Microcrystalline graphite is the main form of natural graphite, composed of numerous tiny graphite crystals (with a size less than 1 μm) that are arranged in a disordered fashion. It is characterized by its high degree of graphitization, fine particle size, and isotropy.[4] In addition, microcrystalline graphite has the advantages of abundant resources, low price, good electrolyte compatibility and high stability. Moreover, it has great potential for application in lithium-ion battery anodes.[5] However, the theoretical specific capacity of microcrystalline graphite anode material is low. Additionally, SEI films are generated during the charging and discharging processes of lithium-ion batteries, resulting in a decrease in the first Coulombic efficiency. These limitations restrict its practical application in lithium-ion batteries..[6] Regarding the above issues, the commonly used modification methods currently include the oxidation method,[7−9] the metal or metal oxide deposition method,[10−12] the carbon coating method[13] and the element doping method.[14] Among these methods, oxidation is a relatively simple and cost-effective approach to modify microcrystalline graphite. By combining oxidation intercalation reactions with expansion treatment, the interlayer spacing of graphite sheets is increased. This helps alleviate the volume expansion of active materials during charge and discharge processes, thereby improving the cycling

Received: December 29, 2024
Revised: March 28, 2025
Accepted: April 1, 2025
Published: April 23, 2025

and rate performance of lithium-ion batteries.[15] Lin et al. synthesized microexpanded graphite featuring engineered internal defects and controllably enlarged interlayer spacing via perchloric acid intercalation.[16] The composite delivered a specific discharge capacity of 397 mAh·g^{-1} at 0.2C, maintained 250 mAh·g^{-1} even at an elevated current density of 1.6C.

The discharge specific capacity of graphite negative electrode material treated with oxidation modification is not high. In order to further improve the lithium storage performance of oxidized microcrystalline graphite, combining it with high specific capacity materials is an effective means. Fe_2O_3, with its advantages of high theoretical specific capacity, abundant resources, low cost, and nontoxicity, is considered one of the most promising anode materials for lithium-ion batteries.[17] Nevertheless, its practical implementation faces three key challenges: (i) substantial volume expansion during lithiation/delithiation, (ii) severe particle agglomeration during cycling, and (iii) intrinsically low electronic conductivity leading to poor rate capability.[18] Current mitigation strategies focus on two principal approaches: First, by constructing nanostructures such as nanosheets,[19] nanowires,[20] and nanotubes,[21] the contact area between the electrode and electrolyte can be increased, promoting charge transfer and enhancing the cycling stability and Coulombic efficiency of Fe_2O_3 during charge−discharge processes. Second, composites can be formed by combining Fe_2O_3 with carbon-based materials such as graphite, graphene, and biomass-derived carbon. This approach improves electrical conductivity, shortens the diffusion distance of Li^+ ions, and mitigates the volume expansion of Fe_2O_3 during charge−discharge cycles.[22] Many Fe_2O_3-graphite composite structures with excellent electrochemical performance have been reported so far. Li et al. synthesized Fe_2O_3/graphene oxide (GO) composites as anode materials for lithium-ion batteries, demonstrating a discharge specific capacity of 890 mAh·g^{-1} after 50 cycles at 1C (1005 mA·g^{-1}).[23] Liu et al. engineered α-Fe_2O_3@C hollow sphere composites, which can enhance the transport efficiency of Li^+ and electrons, improve structural stability and electrical conductivity during charge−discharge cycles, achieving a specific discharge capacity of 700 mAh·g^{-1} after 100 cycles at 1C.[24] However, exploring a simple and effective method to obtain anode materials with excellent electrochemical performance still faces certain challenges. This study employs a simple and highly controllable preparation method, utilizing low-cost and highly cycle-stable microcrystalline graphite as the matrix. By significantly expanding fine-sized, difficult-to-oxidize microcrystalline graphite and then compositing it with Fe_2O_3 nanoparticles to exert a synergistic effect, we aim to obtain a new type of lithium-ion battery anode material with superior comprehensive electrochemical performance.

2. EXPERIMENTAL SECTION

2.1. Experimental Materials. Microcrystalline graphite (fixed carbon content >99.9%), hydrogen peroxide (AR), potassium permanganate (AR) and concentrated sulfuric acid (AR) were prepared for EMG. Iron(III) chloride hexahydrate ($FeCl_3·6H_2O$) (AR) was prepared for EMG/Fe_2O_3 composites. *N*-methyl-pyrrolidone (NMP), poly(vinylidene fluoride) (PVDF) and acetylene black were used for preparing electrode slurry. Solutions were prepared using deionized water (≥18.2 MΩ·cm).

2.2. Chemical Synthesis of EMG. 1.5 g of Microcrystalline graphite (MG) was added to a beaker containing 23 mL concentrated sulfuric acid in an ice−water bath. Then 2.4 g of potassium permanganate was added and stirred for 30 min. Afterward, the mixture was transferred to a 35 °C water bath and stirred for an additional 30 min. Deionized water was added for dilution. When the temperature no longer rose, an appropriate amount of hydrogen peroxide was added until no bubbles were produced. After standing for a period of time, high-speed centrifugation was carried out and washed with deionized water until neutral. The product was then dried at 60 °C. After that the EMG was prepared in an Ar atmosphere at 900 °C for 5 min, with a ramp rate of 5 °C/min.

2.3. Chemical Synthesis of EMG/Fe_2O_3. 0.3 g of EMG and an appropriate amount of $FeCl_3·6H_2O$ were placed into beakers with ultrasonicating for 30 min, then transferred to a 60 °C water bath stirring for about 6 h. After standing for a while, the mixtures were separated by suction filtration to obtain the precursors. Finally, with the furnace door closed, the precursors were heated to 500 °C and maintained at that temperature for 2 h in the muffle furnace. EMG and ferric chloride ($FeCl_3$) composites with mass fraction ratios of 1:0.6, 1:1.2 and 1:1.8 were prepared, recorded separately as EMG/Fe_2O_3-1, EMG/Fe_2O_3-2, and EMG/Fe_2O_3-3.

2.4. Structural Characterization. Phase analysis of all materials was performed using powder X-ray diffraction (XRD) with an XRD-6100 instrument. The basic parameters for testing included a Cu Kα radiation source, a tube voltage of 40 kV, a tube current of 30 mA, and a scan rate of 10° min^{-1}. Raman spectroscopy (Sentera R200-L) with a 532 nm laser as the excitation source was used to obtain information on molecular vibrations and crystal structures in the range of 100 to 2000 cm^{-1}. Microscopic morphology and crystal structure of all materials were studied using scanning electron microscopy (SEM; JSM-7500F) and transmission electron microscopy (TEM; JEM-2100F). Chemical bonding states were investigated using X-ray photoelectron spectroscopy (XPS; PHI-5000C ESCA).

2.5. Electrochemical Measurement. CR2035 coin-type cells were assembled for electrochemical testing. To prepare working electrodes with a diameter of 16 mm, the active materials were mixed with carbon black and PVDF binder in a weight ratio of 8:1:1, respectively, using NMP as the blending solvent. The slurry was uniformly coated onto the copper foil current collector with a controlled thickness using a doctor blade and then dried at 105 °C for 6 h in a vacuum oven. After drying, the samples were sectioned into 16 mm diameter electrode disks using a precision slicer. Half-cells were assembled in an argon-filled glovebox, with lithium foils as the counter electrode, polypropylene microporous membranes as separators, 1 M $LiPF_6$ in a mixture of dimethyl carbonate, methyl ethyl carbonate and ethylene carbonate (1:1:1 V/V/V) as the electrolyte. The loading amount of the electrode active materials used in this study is 2.56 mg·cm^{-2}. The BTS-5 V/2.2A battery performance tester was used for charge and discharge testing, within a voltage range of 0.01−3 V (vs Li/Li^+). Cyclic voltammetry (CV) and electrochemical impedance spectroscopy (EIS) measurements were carried out on a CHI660E electrochemical workstation. CV scans were performed between 0.01 and 3 V. EIS measurements were conducted over a frequency range of 0.01 Hz to 100 kHz.

3. RESULTS AND DISCUSSION

3.1. Structural Characterization. The XRD patterns of the pristine MG, EMG and EMG/Fe_2O_3 composite samples

https://doi.org/10.1021/acsomega.4c11654
ACS Omega 2025, 10, 17673−17683

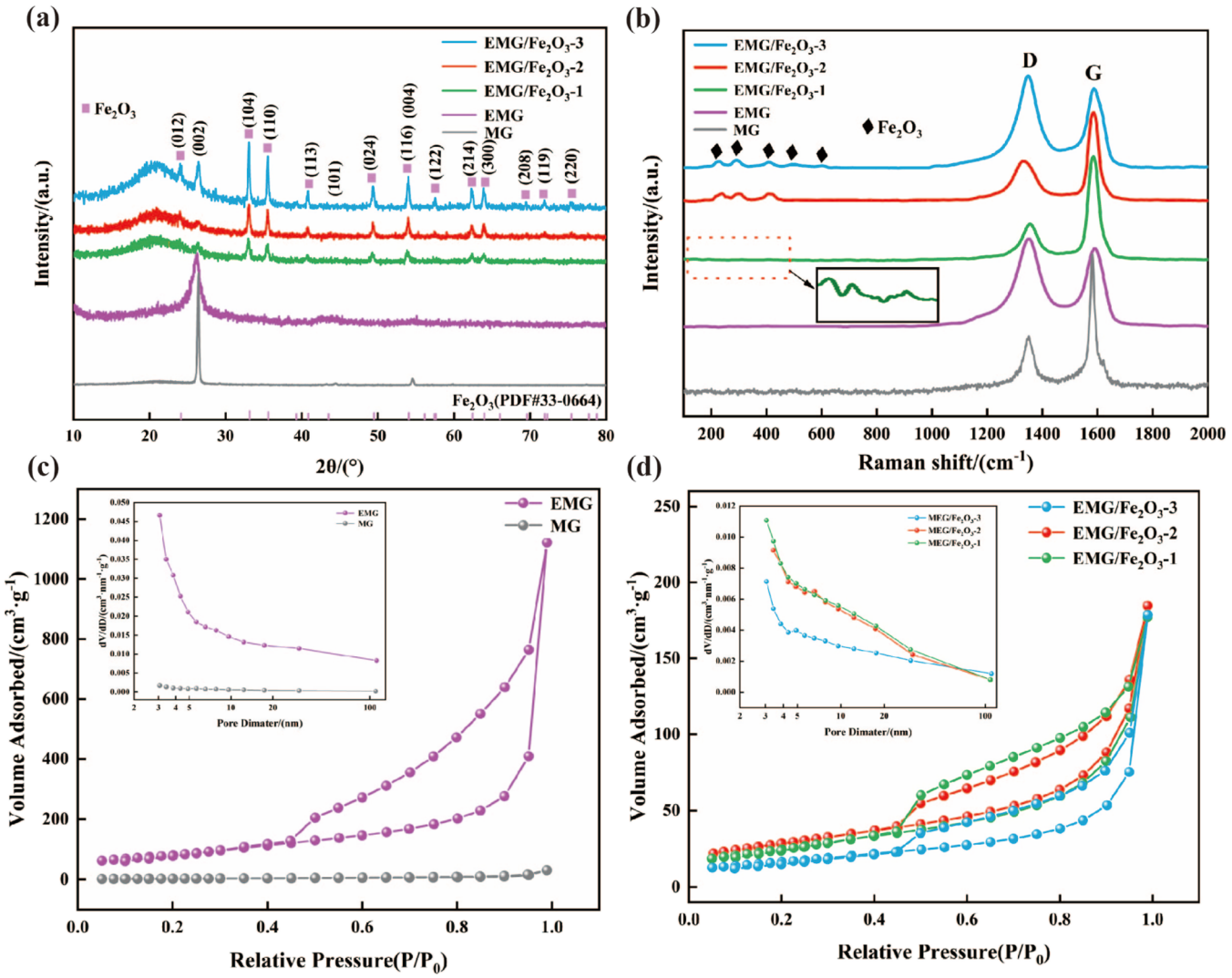

Figure 1. (a) XRD patterns of MG, EMG, EMG/Fe_2O_3-1, EMG/Fe_2O_3-2 and EMG/Fe_2O_3-3; (b) Raman spectra of MG, EMG, EMG/Fe_2O_3-1, EMG/Fe_2O_3-2 and EMG/Fe_2O_3-3; (c) N_2 adsorption−desorption isotherms and pore size distribution of MG and EMG; (d) N_2 adsorption−desorption isotherms and pore size distribution of EMG/Fe_2O_3-1, EMG/Fe_2O_3-2 and EMG/Fe_2O_3-3.

are illustrated in Figure 1a. The peaks at around 26, 44.4, and 54° for the five samples correspond to the characteristic diffraction peaks of graphite on the (002), (101), and (004) crystal planes, respectively. Compared with the XRD patterns of MG, the intensity of the (002) crystal plane diffraction peak is significantly reduced and shifted to the left for EMG. The (101) and (004) diffraction peaks of the graphite microcrystalline structure are relatively broadened. This phenomenon is attributed to the treatment of MG with an oxidizing intercalation agent, which opens up the edges of the carbon layers. During the heat treatment process, the intercalation compound molecules between the carbon layers generate gases, and the originally tight layered structure of graphite is destroyed.[24,25] Fe_2O_3 phases are observed in the XRD patterns of the three synthesized EMG/Fe_2O_3 composite materials. The peaks at 24.1, 33.2, 35.6, 40.8, 49.5, 54.1, 57.4, 62.4, and 64° corresponded to the (012), (104), (110), (113), (024), (116), (122), (214), and (300) planes of Fe_2O_3, respectively. Furthermore, the diffraction peaks of Fe_2O_3 match the PDF card 33−0664. The sharp peaks observed in the EMG/Fe_2O_3 composites indicate a high degree of crystallinity of the composite materials. As the mass fractions of Fe_2O_3 gradually increase, the characteristic peaks intensity of three Fe_2O_3 samples of EMG/Fe_2O_3-1, EMG/Fe_2O_3-2, and EMG/Fe_2O_3-3 are gradually strengthened. The interlayer spacing of the samples was calculated using the Bragg eq ($2d \sin\theta = n\lambda$), as shown in Table S1. The interlayer spacing of the EMG increases because during the intercalation process, the oxidant is inserted into the layers of graphite, altering the original interlayer structure. Additionally, after the intercalated graphite is calcined at high temperatures, the substances inserted between the layers decompose to produce gases such as oxygen, resulting in an expansion of the interlayer spacing. As the mass fraction of Fe_2O_3 increases, the interlayer spacing first increases and then decreases. This may be due to the fact that an appropriate amount of Fe_2O_3 particles helps to increase the interlayer spacing, but when the content is too high, its nanoparticles tend to accumulate and agglomerate. The grain sizes of the five materials were calculated using the Scherrer formula ($D = K\lambda/(\beta\cos\theta)$), as shown in Table S1. After expansion treatment, the grain size of MG decreases. This may be due to the fact that under the action of an oxidant, MG undergoes mechanical forces such as compression and shearing, leading to the crushing and refinement of the

https://doi.org/10.1021/acsomega.4c11654
ACS Omega 2025, 10, 17673−17683

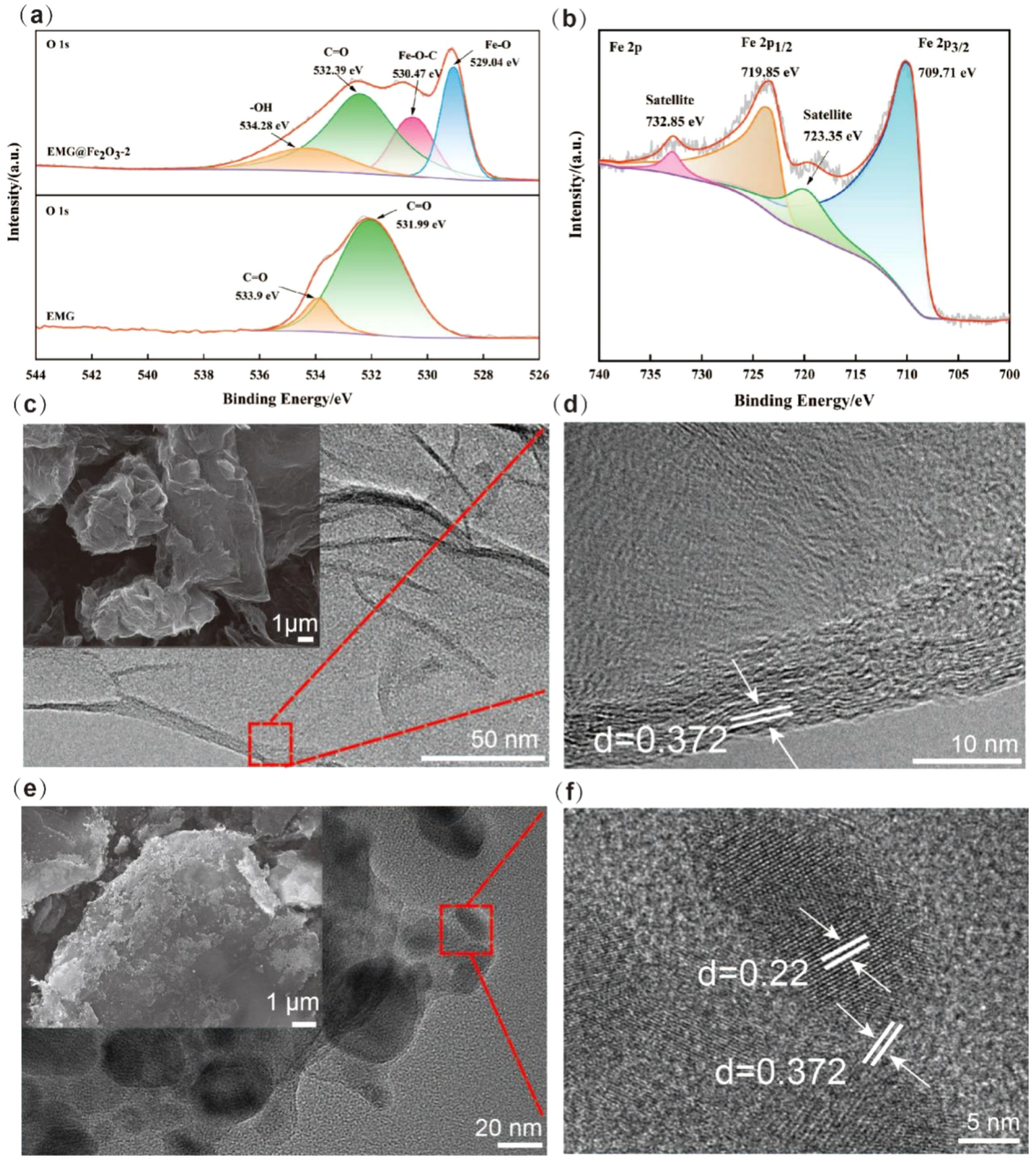

Figure 2. (a) High-resolution C 1s XPS of EMG and EMG/Fe_2O_3-2; (b) high-resolution Fe 2p XPS EMG/Fe_2O_3-2; (c) SEM and TEM images of EMG; (d) HRTEM images of EMG; (e) SEM and TEM images of EMG/Fe_2O_3-2; (f) HRTEM images of EMG/Fe_2O_3-2.

graphite grains, and consequently resulting in a reduction in grain size. The grain size of the composite material first decreases and then increases, which may be attributed to the interfacial interaction between Fe_2O_3 and graphite that promotes grain refinement. Consequently, at low Fe_2O_3 concentrations, the grain sizes of the composite materials tend to be smaller.

The Raman spectra of the MG, EMG, EMG/Fe_2O_3-1, EMG/Fe_2O_3-2, and EMG/Fe_2O_3-3 samples are presented in Figure 1b. The ratio of I_D/I_G is directly proportional to the degree of carbon disorder.[26] As shown in the enlarged view of Figure 1b, there are characteristic peaks of Fe_2O_3 in the composite materials.[27] The D and G peaks remain in their original positions in the EMG, indicating that the structural changes in the EMG during the preparation process are insignificant.[28] The I_D/I_G ratios of all samples are shown in Table S1 (Supporting Information). The I_D/I_G ratios of EMG is higher than that of MG. This is because during the heat treatment process of expanded graphite, the interaction forces between the graphite layers are altered, causing some layers to peel off or rearrange, thereby increasing the defects and disorder within the material. The I_D/I_G ratios of three EMG/Fe_2O_3 composite materials are lower than those of EMG, indicating an increase in the crystallinity of the composite materials. This is due to the higher crystallinity of Fe_2O_3, which, when combined with EMG, reduces the disorder in the composite materials. This is consistent with the XRD analysis results. Figure 1c shows the BET specific surface area tests and BJH pore size distribution curves of MG, and EMG. According to the IUPAC standard, all five samples exhibit type IV isotherms with H3 hysteresis loops, which are characteristic curves of most mesoporous materials.[28] When the relative

https://doi.org/10.1021/acsomega.4c11654
ACS Omega 2025, 10, 17673−17683

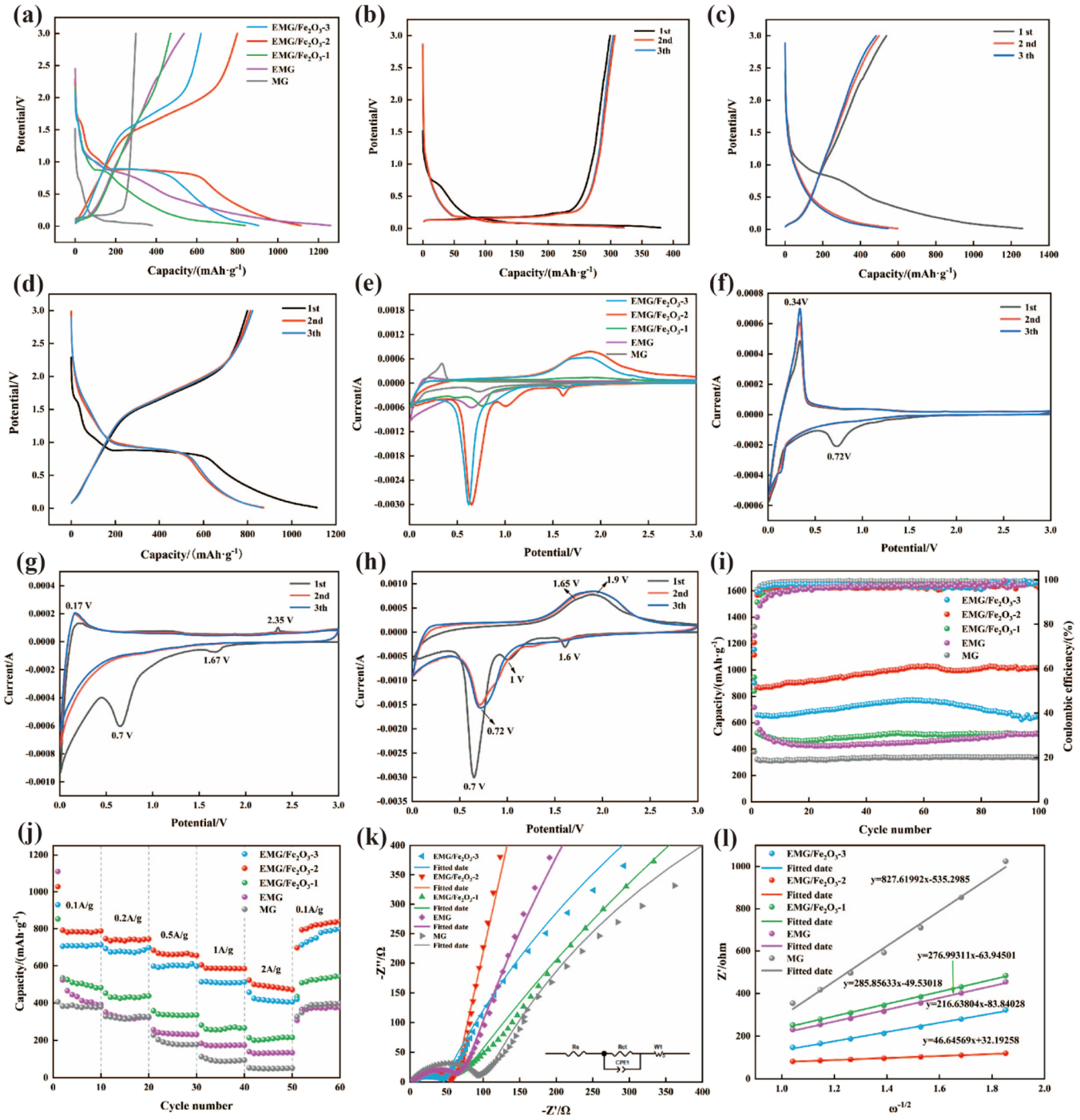

Figure 3. (a) First charge−discharge curves of MG, EMG, EMG/Fe_2O_3-1, EMG/Fe_2O_3-2 and EMG/Fe_2O_3-3; first three charge−discharge curves of the prepared samples MG (b), EMG (c), EMG/Fe_2O_3-2 (d); (e) first cyclic voltammetry curves of MG, EMG, EMG/Fe_2O_3-1, EMG/Fe_2O_3-2 and EMG/Fe_2O_3-3; first three CV curves of samples MG (f), EMG (g), EMG/Fe_2O_3-2 (h); (i) cycling performance at a current density of 100 mA·g^{-1}, (j) rate capability, (k) EIS curves, (l) $Z'-\omega^{-1/2}$ curves of MG, EMG, EMG/Fe_2O_3-1, EMG/Fe_2O_3-2 and EMG/Fe_2O_3-3.

pressure is between 0.5 and 0.9, the hysteresis loop of EMG is larger than that of MG, indicating an increase in the number of defects. As shown in Table S1, the specific surface area of EMG is larger than that of EG. This indicates that the specific surface area is increased mainly due to the porous structure, which provides more channels and space for lithium-ion transport. Figure 1d shows the BET specific surface area tests and BJH pore size distribution curves of EMG/Fe_2O_3-1, EMG/Fe_2O_3-2, and EMG/Fe_2O_3-3. At low relative pressures, the adsorption amount of N_2 increases slowly. Within the range of 0.5−0.9 relative pressure, a large number of N_2 molecules are allowed to enter the pores because of the presence of mesopores, resulting in a significant increase in the adsorption amount. At a relative pressure of 0.9−1, the amount of N_2 adsorbed may rapidly increase due to porous channels or capillary condensation phenomena.[29] The specific surface areas of the composite materials are shown in Table S1. Among them, the EMG/Fe_2O_3-2 composite material has the highest specific surface area (60.783 $m^2 \cdot g^{-1}$). The pore size distribution curves indicate that the pore size distribution of

https://doi.org/10.1021/acsomega.4c11654
ACS Omega 2025, 10, 17673−17683

the composite materials ranges from 3 to 20 nm, with the majority centered around 3 nm. There are more pores in the 60 to 100 nm range in the EMG/Fe_2O_3-3 sample, which may be due to the increase in pore volume per unit pore size caused by the aggregation of more Fe_2O_3 particles. The rich mesoporous structure of composite materials is beneficial for electrolyte infiltration, lithium-ion diffusion, and charge transfer during charge and discharge processes. When the mass fraction of Fe_2O_3 is moderate, the composite material has the largest specific surface area.

The oxidation states and chemical composition of the EMG and EMG/Fe_2O_3-2 composite were identified using XPS analysis. The XPS survey profile of EMG and EMG/Fe_2O_3-2 in Figure S1a (Supporting Information), confirms the presences of C, O, and Fe in the EMG/Fe_2O_3-2. The XPS spectrum of C 1s is presented in Figure S1b (Supporting Information). The peaks can be divided into C−C (284.76 eV), C−O (285.04 eV), and O−C═O (287.93 eV) peaks according to their different binding energies.[30,31] In the EMG/Fe_2O_3-2 composite material, these three peaks are shifted to 284.6, 285.93, and 290.82 eV, respectively. This may be due to the increased specific surface area of the expanded graphite, which exposes more carbon atoms on the surface. These surface carbon atoms interact easily with Fe_2O_3, resulting in a change in their binding energy. The C−O peak may stem from the C−O−C and C−O−Fe bonds, whereas the O−C═O peak is caused by the oxidation of EMG during the synthesis process. Figure 2a shows the binding energy of the O 1s spectrum, with distinct peaks corresponding to surface carboxyl groups (C═O) and adsorbed water (−OH). For both EMG and EMG/Fe_2O_3-2 samples, the peak is associated with carbonyl groups (C═O) appears at approximately 531 eV, while the peak attributed to adsorbed water (−OH) is observed at around 533 eV.[32] In addition, the peak at 530.47 eV for EMG/Fe_2O_3-2 corresponds to the Fe−O−C bond, while the peak at 529.04 eV belongs to lattice oxygen (Fe−O), indicating the interaction between $Fe^{3+}$and the defects incorporated into the EMG. Figure 2b shows the high-resolution XPS spectrum of Fe 2p. It can be seen from the figure that there are two main peaks at 709.71 and 719.85 eV, which are related to the characteristic Fe $2p_{3/2}$ and Fe $2p_{1/2}$ of Fe^{3+} in Fe_2O_3. There are also two satellite peaks at 723.35 and 732.85 eV, indicating that Fe element mainly exists in the form of Fe^{3+} in the EMG/Fe_2O_3 composite material.[33]

We observed the morphological characteristics of the MG, EMG, EMG/Fe_2O_3-1, EMG/Fe_2O_3-2, and EMG/Fe_2O_3-3 in Figure S2 (Supporting Information). MG exhibits an irregular polygonal structure with a smooth surface devoid of impurities, and the graphite layers are tightly packed, displaying few defects. The overall expansion effect of EMG is good, with clear pleated layers, and there are many honeycomb-like porous structures within the layers. There are defects and delamination phenomena at the edges, and the overall volume expands. This provides a larger contact area for electrolyte ions and avoids the detachment and aggregation of active substances on the composite material during charge and discharge processes. Combined with the transmission electron microscope image in Figure 2c, many irregular wrinkles were observed on the surface of the EMG, which are the layers formed after the graphite undergoes oxidation. Figure 2d shows that the average lattice spacing of the (002) crystal plane was measured to be 0.372 nm, which is greater than the spacing of 0.34 nm for MG. This indicates that the interlayer spacing of graphite has increased due to the action of the oxidant. Figure S2c (Supporting Information)shows that a small amount of Fe_2O_3 is distributed on the surface and edges of EMG/Fe_2O_3-1, and the layered structure of the EMG can be observed. Figure S2e (Supporting Information)is the SEM image of EMG/Fe_2O_3-3. EMG/Fe_2O_3-3 exhibits significant agglomeration due to the presence of more Fe_2O_3 nanoparticles attached within the layers of EMG. This reduces the specific surface area of the composite material and blocks the pore structure of the expanded graphite, leading to a decrease in porosity. The content of Fe_2O_3 particles in EMG/Fe_2O_3-2 is moderate, with some of the particles attached to the surface of the graphite. A part of the Fe_2O_3 particles can be fixed in the layered structure of the EMG, preventing them from aggregating during nucleation and growth. This is beneficial for the dispersion of nanoparticles and their mutual coordination. Based on the TEM observation in Figure 2e. The lighter colored film is an expanded graphite sheet, while the darker colored film is iron oxide. Fe_2O_3 is uniformly loaded on the expanded graphite sheet. Figure 2f shows that the lattice spacing is obtained, where d_1 = 0.372 nm corresponds to the (002) plane of graphite, and d_2 = 0.22 nm corresponds to the (113) plane of Fe_2O_3.[34] This test result is consistent with the XRD results.

3.2. Electrochemical Performance Testing. Figure 3a shows the first charge−discharge profiles of MG, EMG, EMG/Fe_2O_3-1, EMG/Fe_2O_3-2, and EMG/Fe_2O_3-3 at a current density of 100 mA·g^{-1}. Based on Table S2, EMG/Fe_2O_3-2 exhibits the best overall electrochemical performance. As can be seen from Figure 3b, the charge−discharge curve of MG is roughly U-shaped, with a relatively low charge−discharge platform. The first discharge curve has a discharge plateau at 0.72 V, followed by a sharp drop in voltage and another discharge plateau at 0.2 V before stabilizing. Combining the CV curve presented in Figure 3f, we can observe a prominent oxidation peak at 0.34 V, corresponding to the delithiation process of graphite microcrystals and defect structures. The discharge−charge profiles of EMG for the first, second, and 3th cycles at the current rate of 100 mA·g^{-1} are presented in Figure 3c. The specific capacity of EMG during the first three charge−discharge cycles is higher than that of MG. The initial delithiation voltage platform of EMG is approximately 0.7 V. The second and third discharge curves of EMG exhibit a high degree of overlap. The initial charge−discharge curve of EMG shows a higher discharge specific capacity, which can be attributed to the unique honeycomb-like porous structure of the EMG. This structure provides a large number of active sites that facilitate electrochemical reactions. Additionally, the expanded graphite has a large specific surface area, enabling it to adsorb more lithium ions into its interlayer spaces, leading to the formation of more lithium compounds. During the discharge process, a significant amount of electrical energy is released. Combining the CV curve presented in Figure 3g, the peak at approximately 0.7 V in the CV curve of EMG represents the reduction peak of graphite. The small reduction peak at 1.67 V may be attributed to reactions between the electrolyte and oxygen-containing functional groups on the surface of the electrode materials. The reduction peak at 0.65 V corresponds to the decomposition of the electrolyte and the formation process of the SEI film, which disappeared in subsequent cycles, indicating the formation of a stable SEI film and the irreversibility of this reaction process. The oxidation peak at 0.34 V for MG shifts to 0.17 V in EMG, which can be

https://doi.org/10.1021/acsomega.4c11654
ACS Omega 2025, 10, 17673−17683

attributed to the oxidized graphite containing more oxygen-containing functional groups. These functional groups alter the electronic structure and reactivity of the graphite, thereby leading to the shift in the oxidation peak potential. The small oxidation peak appearing at 2.35 V is attributed to the enhanced capacity resulting from the increased pore and interlayer spacing of the expanded graphite. The curves of the second and third cycles exhibit high overlap, which is consistent with the results from the first charge−discharge cycle.

Figure 3d show the first three charge−discharge curves of EMG/Fe_2O_3-2, with distinct discharge platforms at approximately 0.7, 1.0, and 1.6 V. Combining the CV curve presented in Figure 3h, which exhibits three reduction peaks at 0.7, 1.0, and 1.6 V in the first cycle, these peaks correspond to three-step lithiation mechanism.

$$Fe_2O_3 + xLi^+ + xe^- \rightarrow Li_xFe_2O_3 \quad (1)$$

$$Li_xFe_2O_3 + (2 - x)Li^+ + (2 - x)e^- \rightarrow Li_2Fe_2O_3 \quad (2)$$

$$Li_2Fe_2O_3 + 4Li^+ \rightarrow 2Fe^0 + 3Li_2O \quad (3)$$

Specifically, the peak at 1.6 V arises from the insertion of Li^+ into the structure of Fe_2O_3, forming $Li_xFe_2O_3$ without altering the crystal structure (see eq 1). The peak at 1.0 V corresponds to the formation of $Li_2Fe_2O_3$ (see eq 1). The strong reduction peak around 0.7 V is related to the reduction of Fe^{3+} to Fe^0 and the irreversible formation of the SEI film (see eq 1).[35] During the subsequent second and third scans of EMG/Fe_2O_3-2, the two peaks at 1.6 and 1.02 V disappear due to irreversible Li^+ extraction and the phase transition from $Li_xFe_2O_3$ to $Li_2Fe_2O_3$.[36] The oxidation peak at 0.7 V shifts to the right, which is attributed to the changes in the microstructure of the electrode material after the first cycle, making it easier for lithium ions to intercalate. From the second cycle onward, the potential of the reduction peak increases to around 0.72 V, accompanied by a significant decrease in peak intensity, before stabilizing at this voltage.

In Figure 3i, the cyclic performance of MG, EMG, EMG/Fe_2O_3-1, EMG/Fe_2O_3-2, and EMG/Fe_2O_3-3 is shown at a constant current density of 100 mA·g^{-1}. After 100 cycles, the discharge specific capacities are 337.45, 511.38, 515.63, 1007.05, and 653.41 mAh·g^{-1}, respectively, as shown in Table S2. The EMG/Fe_2O_3 −2 exhibits the highest discharge specific capacity. The low initial Coulombic efficiency of EMG may be due to the low initial charge−discharge process. Stress concentration and microcracks within the anode are generated because of uneven insertion and extraction of lithium ions. The capacity retention rate of MG is higher than that of EMG, but the charge−discharge specific capacity is the lowest. The capacity retention rate of the EMG/Fe_2O_3 composite material is higher than that of EMG. This is mainly because the layered structure of expanded graphite is conducive to the high dispersion of Fe_2O_3 particles, preventing their aggregation and detachment, alleviating the volume expansion during the charge−discharge process, and providing support to make the composite material structure more stable. The negative decay phenomenon in the capacity of the composite material during cycling is mainly attributed to the continuous activation of the Fe_2O_3 active component within the pores of the EMG during the charging and discharging processes. As the active sites inside the material gradually become exposed, the composite material is able to better participate in electrochemical reactions, forming abundant pore channels that accelerate the diffusion of lithium ions and continuously increase its lithium storage capacity. When the content of Fe_2O_3 is moderate, it can be well dispersed within the pore structure of expanded graphite. Aggregation phenomena are mitigated for effective dispersion, thereby enhancing the structural stability of the composite. This finding is in good agreement with the SEM analysis.

Figure 3j shows the rate performance of MG, EMG, EMG/Fe_2O_3-1, EMG/Fe_2O_3-2, and EMG/Fe_2O_3-3 under current densities of 0.1, 0.2, 0.5, 1, and 2 A·g^{-1}, and then back to 0.1 A·g^{-1}. As can be seen from Table S2, EMG/Fe_2O_3-2 exhibits the highest discharge specific capacity and rate performance, delivering 808.90, 740.61, 663.76, 587.64, and 489.50 mAh·g^{-1}, respectively, under current densities of 0.1, 0.2, 0.5, 1, and 2 A·g^{-1}. This indicates that EMG/Fe_2O_3-2 exhibits the best rate capability, which can be attributed to the composite of EMG and Fe_2O_3 effectively preventing the performance degradation caused by the volume expansion of Fe_2O_3 during charging and discharging, thereby enhancing the lithium storage capability of the electrode material under high current conditions. The appropriate mass fraction of Fe_2O_3 in the composite materials is crucial for achieving high electrochemical performance in lithium-ion battery anode materials, which is consistent with the analysis of cycling performance. The optimal cycling performance of EMG/Fe_2O_3-2 is primarily attributed to the high theoretical specific capacity of Fe_2O_3 (1007 mAh·g^{-1}). The formation of a micronano composite structure between EMG and Fe_2O_3, combined with the abundant pore structure of EMG, provides volume buffering space for the volume expansion of Fe_2O_3.

The Nyquist plots of MG, EMG, EMG/Fe_2O_3-1, EMG/Fe_2O_3-2, and EMG/Fe_2O_3-3 displayed in Figure 3k, were used to interpret the electron-transfer process across the electrode−electrolyte interface. The initial values of the semicircles in the high-frequency region signify the surface resistance (R_s) values at the electrode/electrolyte interfaces of the samples, and the diameters of the semicircles represent the charge-transfer resistance (R_{ct}) of the samples. The ascending lines following the semicircles in the low-to medium-frequency region represent the diffusion of Li^+. The R_s and R_{ct} values for each sample were determined after fitting the Nyquist plot data using equivalent circuits (inset of Figure 3k), and the results are summarized in Table S2. The straight lines in Figure 3k represent the fittings for each sample.[37,38] The radius of the impedance semicircle in the midto-high frequency region for the EMG is smaller than that of MG. Additionally, the slope of the straight line is steeper, indicating that the impedance of the EMG is lower. A lower resistance is beneficial for improving the rate performance. The EMG/Fe_2O_3-3 electrode exhibits the smallest semicircle diameter, indicating that its charge-transfer R_{ct} is lower than of the other three samples. This could be attributed to the high proportion of Fe_2O_3 in EMG/Fe_2O_3-3, which enhances electron transfer efficiency, leading to reduced impedance. EMG/Fe_2O_3-2 has the largest slope, and its R_{ct} value is second only to that of EMG/Fe_2O_3-3. Moreover, the R_{ct} values of all three composites are higher than that of EMG, suggesting that the doping of Fe_2O_3 not only enhance the lithium storage capacity of the electrode material but also effectively improves the formation process of the SEI by generating a more stable conductive film. This contributes to increasing the specific capacity of lithium-ion batteries and enhancing the reversibility of electrochemical reactions.

https://doi.org/10.1021/acsomega.4c11654
ACS Omega 2025, 10, 17673−17683

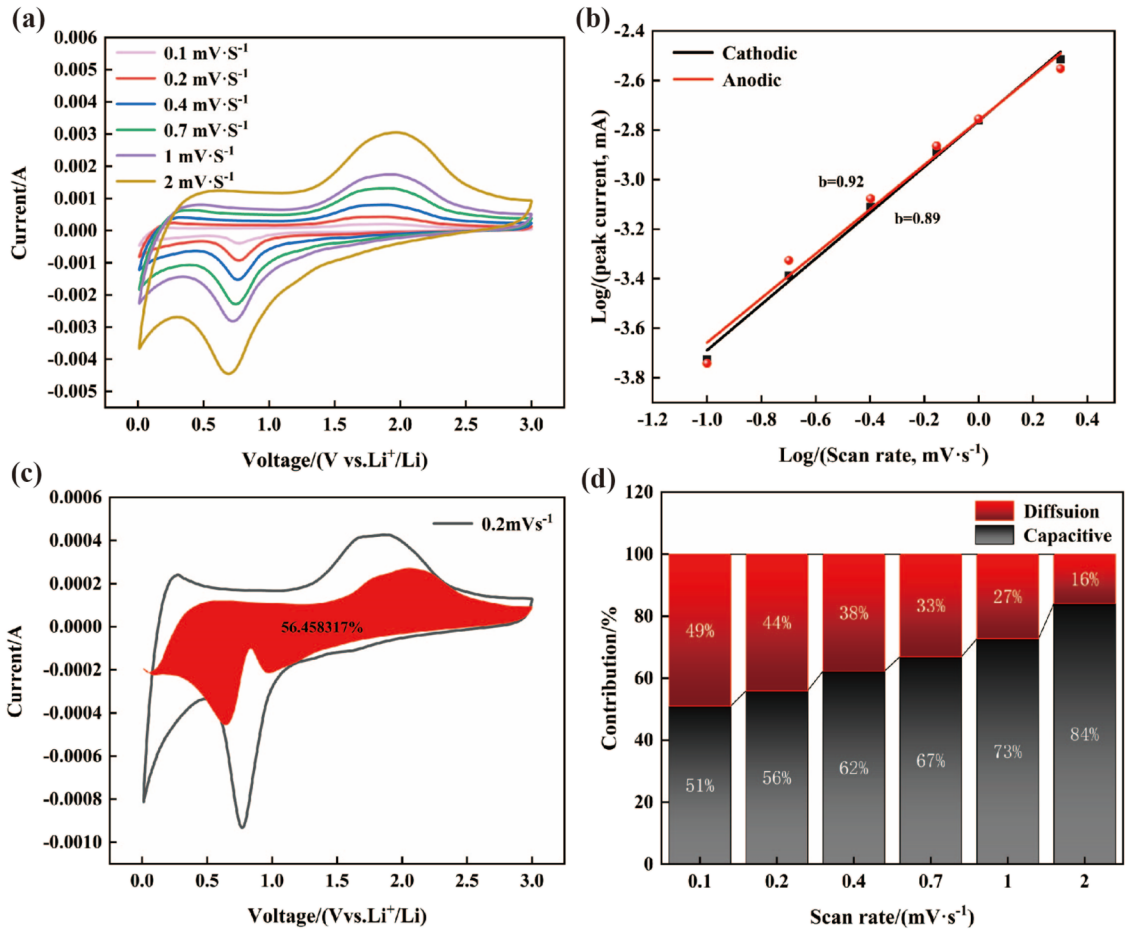

Figure 4. (a) CV of EMG/Fe_2O_3-2 curves at various scan rates from 0.1 to 2.0 mV·s^{-1}, (b) value of b EMG/Fe_2O_3-2 at oxidation peak and reduction peak, (c) contribution of capacitance to the total capacity at a scan rate of 0.2 mV s^{-1} for EMG/Fe_2O_3-2, (d) ratios of capacitance and diffusion contribution for EMG/Fe_2O_3-2 at different scan rates.

Furthermore, the lithium-ion diffusion rate within the electrode is estimated by calculating the Warburg factor (σ), which is inversely proportional to the ion diffusion efficiency, as shown in Figure 3l. The lithium-ion diffusion coefficient (D_{Li^+}) for the five anode materials is calculated using the following formula: $D_{Li^+} = R^2T^2/(2A^2n^4F^4C^2\sigma^2)$, where R is the universal gas constant, T is the absolute temperature, A is the electrochemical reaction surface area, n represents the number of electrons transferred, F is the Faraday constant, C is the concentration of Li^+, and σ represents the Warburg factor. The value of Z' is calculated using the formula $Z' = R_s + R_{ct} + \sigma\omega^{-1/2}$.[39,40] As shown in Table S2, the D_{Li^+} value for EMG/Fe_2O_3-2 is significantly higher, at 7.43×10^{-16}, which is notably larger than the other four anode materials. The high lithium-ion diffusion coefficient of EMG/Fe_2O_3-2 demonstrates excellent diffusion kinetics, indicating an optimal balance between charge-transfer resistance and ion diffusion rate. In the composite materials of Fe_2O_3 and graphite, graphite acts as a conductive agent, enhancing the electrical conductivity of the composites. When the interlayer spacing is expanded, more Fe_2O_3 nanoparticles are doped between the layers, leading to a synergistic effect between the two.

3.3. Analysis of Lithium Storage Mechanism. To further investigate the lithium storage mechanism of the EMG/Fe_2O_3-2 electrode material, the reaction kinetics of EMG/Fe_2O_3-2 were studied by determining the relationship between the peak current (i) and the scan rate (v) at various scan rates. Figure 4a shows the CV curves at different scan rates ranging from 0.1 to 2 mV s^{-1}. In the CV curves, the cathodic and anodic peaks represent the insertion and extraction behaviors of Li^+. As the scan rate increases, these peaks shift toward lower and higher potentials, respectively, resulting in a potential difference. This leads to increased polarization, which degrades electrochemical performance and electrode reaction kinetics. For the EMG/Fe_2O_3-2 electrode, even at the relatively high scan rate of 2 mV s^{-1}, the CV curves retain distinct redox peaks, indicating good reversibility and excellent electrochemical performance.

The relationship between the current (i) in the CV curves and the corresponding scan rate (v) can be expressed mathematically using this equation

$$i = av^b \tag{4}$$

The value of b, a tunable parameter ranging from 0.5 to 1.0, can be determined by plotting the slope of the fitted line between $\log(i)$ and $\log(v)$.[41] As shown in Figure 4b, the cathodic and anodic reaction processes of the EMG/Fe_2O_3-2 electrode exhibit a suppressed capacitive-dominated behavior, with relatively high b-values of 0.89 and 0.92, respectively. This indicates that the electrode material possesses a combination of capacitive and diffusion-controlled characteristics, making it suitable for use as a lithium-ion battery electrode material.

https://doi.org/10.1021/acsomega.4c11654
ACS Omega 2025, 10, 17673−17683

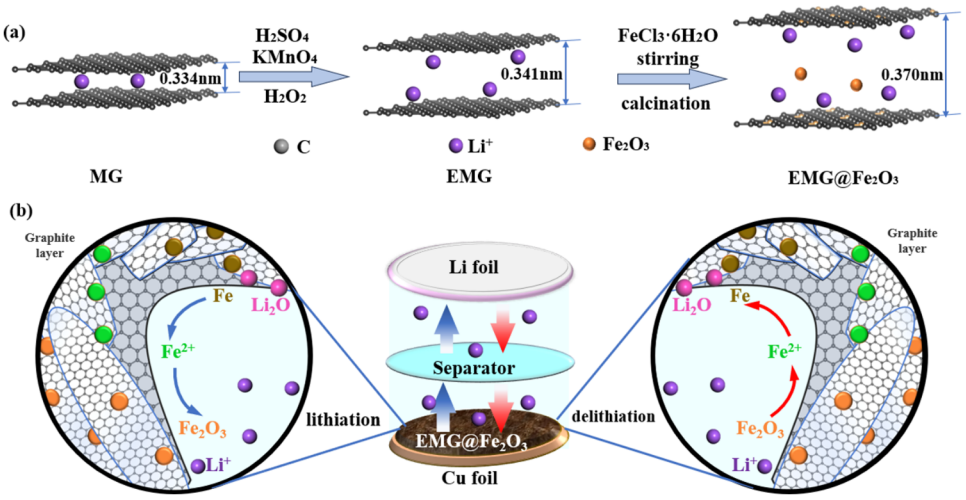

Figure 5. (a) Crystal structures of MG, EMG, and EMG/Fe_2O_3-2, (b) lithium storage mechanism diagram of EMG/Fe_2O_3.

At a fixed scan rate, the contribution of the capacitive and diffusion-controlled components can be analyzed using the following formula

$$i = k_1 v + k_2 v^{1/2} \tag{5}$$

In eq 5, $k_1 v$ and $k_2 v^{1/2}$ correspond to the capacitive and diffusion-controlled contributions, respectively, at a specific potential.[42] As shown in Figure 4c, at a scan rate of 0.2 $mV \cdot s^{-1}$, the capacitive contribution accounts for 56.5% of the total current. Equation 5 can be rearranged as

$$i/v^{1/2} = k_1 v^{1/2} + k_2 \tag{6}$$

k_1 and k_2 can be determined by plotting the slope and intercept of the $i/v^{1/2}$ versus $v^{1/2}$ function graph, respectively.[43] The contributions of capacitive and diffusion-controlled components are presented in the histogram of Figure 4d, showing the capacitive contribution rates at various scan rates. As the scan rate increases, the capacitive contribution gradually increases from 51 to 84%. The high capacitive contribution indicates that Li^+ are efficiently adsorbed, facilitating rapid lithiation and delithiation reactions. The short diffusion path of Li^+ helps avoid structural damage to the active materials, thereby providing excellent electrochemical performance.

Under the action of an oxidant, the interlayer spacing of expanded graphite increases, and numerous pore defects are generated. The addition of Fe_2O_3 in the EMG/Fe_2O_3 composite material further enlarges the interlayer spacing, which is conducive to increasing the lithium storage space and improving the lithium storage capacity, as shown in Figure 5a. The incorporation of Fe_2O_3 generates iron ions with different valence states, enhancing ionic conductivity. However, iron tends to undergo significant volume expansion during charging and discharging processes. Based on specific surface area analysis, the pore diameters of EMG/Fe_2O_3-2 are primarily distributed between 3 and 20 nm. Microscopic observations reveal that the particle size of Fe_2O_3 ranges from 10 to 20 nm, indicating that the porous structure of EMG not only serves as a reservoir for iron ions but also acts as a confining space to mitigate the volume expansion effect of iron ions, thereby stabilizing the structure of the composite material. As shown in Figure Figure 5b, in this work, the prepared composite material was studied using a lithium foil as the counter electrode in a half-cell discharge configuration. During the electrochemical reaction occurring at the electrode, Li^+ from the electrolyte penetrate into the composite material through the separator. Simultaneously, Fe^{3+} in the Fe_2O_3 on the electrode surface is reduced to Fe^{2+} and ultimately to free Fe atoms. During the charging process, an SEI film is formed, covering the surfaces of EMG and Fe_2O_3 particles, and Li^+ are extracted from the composite electrode. The overall reversible reaction can be summarized as follows

$$Fe_2O_3 + 6Li^+ + 6e^- \rightleftarrows 3Li_2O + 2Fe \tag{7}$$

During the discharge reaction, the iron in Fe_2O_3 primarily exists in ionic form, which not only enhances the ionic conductivity but also effectively suppresses the growth of lithium dendrites caused by elemental iron. Consequently, the risk of separator puncture and short-circuiting is mitigated, leading to a notable improvement in the safety of lithium-ion batteries. On the other hand, iron ions possess more electron orbitals for activity compared to lithium ions, allowing electrons to be better accommodated during the discharge process. This is a crucial factor contributing to the enhanced specific capacity of the battery after doping with trivalent iron. Moreover, during the cycling process of the composite material, there is an upward trend in the discharge specific capacity. This can be attributed to the fact that the porous structure of expanded graphite restricts the complete activation of Fe^{3+} in Fe_2O_3 during the initial discharge stage. As the reaction progresses, Fe^{3+} and Li^+ shuttle repeatedly between the two electrodes, gradually activating the active components of Fe_2O_3. This acceleration of the diffusion of lithium ions and iron ions leads to a continuous increase in the lithium storage capacity.

4. CONCLUSIONS

In summary, this work employs high-purity and structurally stable EMG as the matrix and uses $FeCl_3 \cdot 6H_2O$ as the iron source. Through methods such as hydrothermal reaction and high-temperature calcination, EMG/Fe_2O_3 micronanostructured composite materials with high electrochemical performance are prepared. The EMG/Fe_2O_3-2 composite exhibits the most excellent electrochemical performance, with a reversible specific capacity of 1007.05 $mAh \cdot g^{-1}$ at a current density of 0.1 $A \cdot g^{-1}$ after 100 cycles. Mechanism analysis indicates that the porous structure of EMG not only provides more ion storage

https://doi.org/10.1021/acsomega.4c11654
ACS Omega 2025, 10, 17673−17683

sites but also acts as a confining space to mitigate the volume expansion of Fe_2O_3, thereby stabilizing the structure of the composite material. The introduction of Fe_2O_3 enhances the ionic conductivity of lithium-ion batteries, and as the reaction progresses, the active components of Fe_2O_3 are gradually activated, leading to an increasing trend in lithium storage capacity. Reaction kinetics studies show that EMG/Fe_2O_3-2 has a high capacitive contribution rate, which enables effective adsorption of Li^+ and rapid lithiation/delithiation reactions, thereby shortening the diffusion path of Li^+. Based on these conclusions, this study not only significantly improves the electrochemical performance of graphite-based anode materials for lithium-ion batteries, but also offers important insights into the lithium storage mechanism of anode materials, holding great potential for application in the field of high-capacity lithium-ion batteries.

■ ASSOCIATED CONTENT

Supporting Information

The Supporting Information is available free of charge at https://pubs.acs.org/doi/10.1021/acsomega.4c11654.

XPS survey profile of EMG and EMG/Fe_2O_3-2 in Figure S1(a), which confirms the presence of C, O, and Fe in the EMG/Fe_2O_3-2 sample. The high-resolution XPS spectrum of the O 1s 2p region for EMG/Fe_2O_3-2 is presented in Figure S1(b). The peaks observed can be categorized into C−C (at 284.76 eV), C−O (at 285.04 eV), and O−C═O (at 287.93 eV) peaks based on their distinct binding energies. The SEM images of MG, EMG, and the composites EMG/Fe_2O_3-1, EMG/Fe_2O_3-2, and EMG/Fe_2O_3-3 are shown in Figure S2. MG exhibits an irregular polygonal structure with a smooth surface, free of impurities, and the graphite layers are tightly packed, displaying minimal defects, as observed in Figure S2(a). The overall expansion effect of EMG is good, with clear pleated layers and numerous honeycomb-like porous structures within the layers, as depicted in Figure S2(b). A small amount of Fe_2O_3 is distributed on the surface and edges of EMG in the case of EMG/Fe_2O_3-1, and the layered structure of the EMG is still discernible, as seen in Figure S2(c). In EMG/Fe_2O_3-2, the content of Fe_2O_3 particles is moderate, with some particles attached to the surface of the graphite, as illustrated in Figure S2(d). Finally, EMG/Fe_2O_3-3 exhibits significant agglomeration due to the presence of a higher number of Fe_2O_3 nanoparticles attached within the layers of EMG, as shown in Figure S2(e). The structural characterization data for MG, EMG, and the composites EMG/Fe_2O_3-1, EMG/Fe_2O_3-2, and EMG/Fe_2O_3-3 are presented in Table S1. These data include the d_{002} spacing, grain size, disorder degree, specific surface area, and pore volume. The electrical performance data for these materials are provided in Table S2, encompassing the first discharge specific capacity, first Coulombic efficiency, capacity retention after 100 cycles, capacity retention at a current density of $2A{\cdot}g^{-1}$, R_{ct}, and D_{Li^+} (PDF)

■ AUTHOR INFORMATION

Corresponding Author

Sen Yang − *College of Material Science and Engineering, Liaoning Technical University, FuXin 123000, China;* orcid.org/0000-0002-0281-6818; Email: sanmuziysys@163.com

Authors

Ning Zhao − *College of Material Science and Engineering, Liaoning Technical University, FuXin 123000, China*

Kang Zheng − *College of Material Science and Engineering, Liaoning Technical University, FuXin 123000, China*

Lu Sun − *College of Material Science and Engineering, Liaoning Technical University, FuXin 123000, China*

Jiahui Niu − *College of Material Science and Engineering, Liaoning Technical University, FuXin 123000, China*

Complete contact information is available at: https://pubs.acs.org/10.1021/acsomega.4c11654

Notes

The authors declare no competing financial interest.

■ ACKNOWLEDGMENTS

The authors gratefully acknowledge the financial support from the Research Projects of the Education Department of Liaoning Province (Grant Nos: JYTMS20230800; LN2019JL026).

■ REFERENCES

(1) Quilty, C. D.; Wu, D.; Li, W.; Bock, D. C.; Wang, L.; Housel, L. M.; Abraham, A.; Takeuchi, K. J.; Marschilok, A. C.; Takeuchi, E. S. Electron and ion transport in lithium and lithium-ion battery negative and positive composite electrodes. *Chem. Rev.* **2023**, *123* (4), 1327−1363.

(2) Song, Y.; Wang, L.; Sheng, L.; Ren, D.; Liang, H.; Li, Y.; Wang, A.; Zhang, H.; Xu, H.; He, X. The significance of mitigating crosstalk in lithium-ion batteries: a review. *Energy Environ. Sci.* **2023**, *16* (5), 1943−1963.

(3) Ding, X.; Zhou, Q.; Li, X.; Xiong, X. Fast-charging anode for lithium ion batteries: progress and challenges. *Chem. Commun.* **2024**, *60*, 2472−2488.

(4) Peng, J.; Tan, H.; Wu, Z.; Tang, Y.; Liu, P.; He, L.; Yang, J.; Hu, S.; Wang, S.; Wang, X. Improving natural microcrystalline graphite performances by a dual modification strategy toward practical application of lithium ion batteries. *ACS Appl. Mater. Interfaces* **2023**, *15* (51), 59552−59560.

(5) Huang, P.; Liu, B.; Zhang, J.; Liu, M.; Xie, Z. Silicon/carbon composites based on natural microcrystalline graphite as anode for lithium-ion batteries. *Ionics* **2021**, *27*, 1957−1966.

(6) Yu, Y.; Yang, Z.; Liu, Y.; Xie, J. Achieving SEI preformed graphite in flow cell to mitigate initial lithium loss. *Carbon* **2022**, *196*, 589−595.

(7) Xiang, F.; Hou, W.; Gu, X.; Wen, L.; Sun, Y.; Lu, W. One-pot synthesis of MnO-loaded mildly expanded graphite composites as high-performance lithium-ion battery anode materials. *J. Alloys Compd.* **2022**, *897*, No. 163202, DOI: 10.1016/j.jallcom.2021.163202.

(8) Zhang, J.; Lei, Y.; Lin, Z.; Xie, P.; Lu, H.; Xu, J. A novel approach to recovery of lithium element and production of holey graphene based on the lithiated graphite of spent lithium ion batteries. *Chem. Eng. J.* **2022**, *436*, No. 135011.

(9) Chen, X.; Xiao, F.; Lei, Y.; Lu, H.; Zhang, J.; Yan, M.; Xu, J. A novel approach for synthesis of expanded graphite and its enhanced lithium storage properties. *J. Energy Chem.* **2021**, *59*, 292−298.

(10) Ma, H.; Yu, Z.; Chen, J.; Wang, D.; Dong, C.; Mao, Z. Incorporating α-Al_2O_3 nanodots into expanded graphite anodes toward stable fast charging for lithium-ion batteries. *ACS Appl. Energy Mater.* **2023**, *6* (3), 1389−1395.

(11) Jiang, J.; Liu, J.; Chen, Y.; Sun, R.; Liu, Y.; Yang, Y.; Yang, Y.; Yang, G. Preparation of hierarchical hexagonal nanoplates NiO

composite with microcrystalline graphite for highly reversible lithium storage. *J. Alloys Compd.* **2020**, *815*, No. 152333.
(12) Sandhya, C. P.; Bibin, J.; Gouri, C. $Sn/Al_2O_3/C/CNT$ composite prepared by wet milling as anode material for lithium-ion cells. *J. Sci.: Adv. Mater. Devices* **2017**, *2* (2), 210−214.
(13) Xiao, Y.; Li, J.; Huang, W.; Wang, L.; Luo, J. Green & efficient regeneration of graphite anode from spent lithium ion batteries enabled by asphalt coating. *J. Mater. Sci.: Mater. Electron.* **2022**, *21*, 16740−16752.
(14) Yang, X.; Zhen, H.; Liu, H.; Chen, C.; Zhong, Y.; Yang, X.; Wang, X.; Yang, L. Environmental-friendly and effectively regenerate anode material of spent lithium-ion batteries into high-performance P-doped graphite. *Waste Manage.* **2023**, *161*, 52−60.
(15) Lee, Y.; Jeghan, S. M. N.; Lee, G. Boost charging lithium-ion battery using expanded graphite anode with enhanced performance. *Mater. Lett.* **2021**, *299*, No. 130077.
(16) Lin, Y.; Huang, Z.; Yu, X.; Shen, W.; Zheng, Y.; Kang, F. Mildly expanded graphite for anode materials of lithium-ion battery synthesized with perchloric acid. *Electrochim. Acta* **2014**, *116*, 170−174.
(17) Zhang, G.; Shi, Y.; Wang, H.; Jiang, L.; Yu, X.; Jing, S.; Xing, S.; Tsiakaras, P. A facile route to achieve ultrafine Fe_2O_3 nanorods anchored on graphene oxide for application in lithium-ion battery. *J. Power Sources* **2019**, *416*, 118−124.
(18) Ma, L.; Wang, Z.; Tian, S.; Liu, X.; Li, Z.; Huang, J.; Deng, X.; Huang, Y. The α-Fe_2O_3/graphite anode composites with enhanced electrochemical performance for lithium-ion batteries. *Nanotechnology* **2020**, *31* (43), No. 435404.
(19) Wang, Y.; Han, J.; Gu, X.; Dimitrijev, S.; Hou, Y.; Zhang, S. Ultrathin Fe_2O_3 nanoflakes using smart chemical stripping for high performance lithium storage. *J. Mater. Chem. A* **2017**, *5* (35), 18737−18743.
(20) Wang, H.-g.; Zhou, Y.; Shen, Y.; Li, Y.; Zuo, Q.; Duan, Q. Fabrication, formation mechanism and the application in lithium-ion battery of porous Fe_2O_3 nanotubes via single-spinneret electrospinning. *Electrochim. Acta* **2015**, *158*, 105−112.
(21) Park, S. K.; Park, G. D.; Kang, Y. C. Three-dimensional porous microspheres comprising hollow Fe_2O_3 nanorods/CNT building blocks with superior electrochemical performance for lithium-ion batteries. *Nanoscale* **2018**, *10* (23), 11150−11157.
(22) Xu, B.; Guan, X.; Zhang, L. Y.; Liu, X.; Jiao, Z.; Liu, X.; Hu, X.; Zhao, X. S. A simple route to preparing γ-Fe_2O_3/RGO composite electrode materials for lithium ion batteries. *J. Mater. Chem. A* **2018**, *6* (9), 4048−4054.
(23) Li, H.; Zhu, X.; Sitinamaluwa, H.; Wasalathilake, K.; Xu, L.; Zhang, S.; Yan, C. Graphene oxide wrapped Fe_2O_3 as a durable anode material for high-performance lithium-ion batteries. *J. Alloys Compd.* **2017**, *714*, 425−432.
(24) Liu, R.; Zhang, C.; Wang, Q.; Shen, C.; Wang, Y.; Dong, Y.; Zhang, N.; Wu, M. Facile synthesis of α-Fe_2O_3@ C hollow spheres as ultra-long cycle performance anode materials for lithium ion battery. *J. Alloys Compd.* **2018**, *742*, 490−496.
(25) Wang, J.; Yang, X.; Wang, Y.; Jin, S.; Cai, W.; Liu, B.; Ma, C.; Liu, X.; Qiao, W.; Ling, L. Rational design and synthesis of sandwich-like reduced graphene oxide/Fe_2O_3/N-doped carbon nanosheets as high-performance anode materials for lithium-ion batteries. *Chem. Eng. Sci.* **2021**, *231*, No. 116271.
(26) Sang, J.; Zhang, X.; Liu, K.; Cao, G.; Guo, R.; Zhang, S.; Wu, Z.; Zhang, Y.; Hou, R.; Shen, Y.; Shao, G. Effective coupling of amorphous selenium phosphide with high-conductivity graphene as resilient high-capacity anode for sodium-ion batteries. *Adv. Funct. Mater.* **2023**, *33* (19), No. 2211640.
(27) Li, Z.; Zhang, C.; Han, F.; Zhang, F.; Zhou, D.; Xu, S.; Liu, H.; Li, X.; Liu, J. Improving the cycle stability of $FeCl_3$-graphite intercalation compounds by polar Fe_2O_3 trapping in lithium-ion batteries. *Nano Res.* **2019**, *12*, 1836−1844.
(28) Ma, L.; Wang, Z.; Tian, S.; Liu, X.; Li, Z.; Huang, J.; Deng, X.; Huang, Y. The α-Fe_2O_3/graphite anode composites with enhanced electrochemical performance for lithium-ion batteries. *Nanotechnology* **2020**, *31* (43), No. 43540.
(29) Huang, Y.; Lin, Z.; Zheng, M.; Wang, T.; Yang, J.; Yuan, F.; Lu, X.; Liu, L.; Sun, D. Amorphous Fe_2O_3 nanoshells coated on carbonized bacterial cellulose nanofibers as a flexible anode for high-performance lithium ion batteries. *J. Power Sources* **2016**, *307*, 649−656.
(30) Qi, H.; Huang, J.; Tang, L.; Ma, M.; Deng, W.; Zhang, C. Confined pulverization promoting durable pseudocapacitance for FeOOH@ PEDOT anode in Li-ion battery. *J. Electroanal. Chem.* **2021**, *882*, No. 115005.
(31) Santhoshkumar, P.; Prasanna, K.; Jo, Y. N.; Sivagami, I. N.; Kang, S. H.; Lee, C. W. A facile and highly efficient short-time homogenization hydrothermal approach for the smart production of high-quality α-Fe_2O_3 for rechargeable lithium batteries. *J. Mater. Chem. A* **2017**, *5*, 16712−16721.
(32) Qi, H.; Cao, L.; Li, J.; Huang, J.; Ma, M.; Cheng, Y.; Wang, C.; Dang, H. Rice crust-like Fe_3O_4@C/rGO with improved extrinsic pseudocapacitance for high-rate and long-life Li-ion anodes. *J. Alloys Compd.* **2019**, *804*, 57−64.
(33) Ma, Y.; Song, X.; Ge, X.; Zhang, H.; Wang, G.; Zhang, Y.; Zhao, H. In situ growth of α-Fe_2O_3 nanorod arrays on 3D carbon foam as an efficient binder-free electrode for highly sensitive and specific determination of nitrite. *J. Mater. Chem. A* **2017**, *5* (9), 4726−4736.
(34) Zhang, D.; Zhang, W.; Zhang, S.; Ji, X.; Le, L. Synthesis of expanded graphite-based materials for application in lithium-based batteries. *J. Energy Storage* **2023**, *60*, No. 106678.
(35) Park, C.; Edmund, E. S.; Bhavana, J.; Taegun, K.; Ail, A.; Mohamed, E. N.; Woo, Y. Y.; Sam, S. Y. Supersonically sprayed Fe_2O_3/C/CNT composites for highly stable Li-ion battery anodes. *Chem. Eng. J.* **2020**, *395*, No. 125018.
(36) Li, L.; Li, Z.; Fu, W.; Li, F.; Wang, J.; Wang, W. α-Fe_2O_3@ C nanorings as anode materials for high performance lithium ion batteries. *J. Alloys Compd.* **2015**, *647*, 105−109.
(37) Huang, Y.; Peng, J.; Luo, J.; Li, W.; Wu, Z.; Shi, M.; Li, X.; Li, N.; Chang, B.; Wang, X. Spherical Gr/Si/GO/C composite as high-performance anode material for lithium-ion batteries. *Energy Fuels* **2020**, *34* (6), 7639−7647.
(38) Liu, J.; L, Y.; Chen, X.; Tang, Y.; Zang, Z.; Zou, C.; Zeng, P.; Li, D.; Xia, J.; Ni, S.; Wang, X. Construction and interfacial modification of a β-$PbSnF_4$ electrolyte with high intrinsic ionic conductivity for a room-temperature fluoride-ion battery. *ACS Appl. Mater. Interfaces* **2023**, *15* (30), 36373−36383.
(39) Peng, J.; Li, W.; Wu, Z.; Li, H.; Zeng, P.; Chen, G.; Chang, B.; Zhang, X.; Wang, X. Si/C composite embedded nano-Si in 3D porous carbon matrix and enwound by conductive CNTs as anode of lithium-ion batteries. *Sustainable Mater. Technol.* **2022**, *32*, No. e00410.
(40) Peng, J.; Li, W.; Wu, Z.; Li, H.; Huang, Y.; Ouyang, Y.; Wang, Y.; Guo, X.; Chen, G.; Wang, X. Rational design and performance of anode materials based on $Si/SiO_x/C$ particles anchored on graphene sheets. *ACS Appl. Energy Mater.* **2021**, *4* (5), 4966−4975.
(41) Wang, J.; Polleux, J.; Lim, J.; Dunn, B. Pseudocapacitive contributions to electrochemical energy storage in TiO_2 (anatase) nanoparticles. *J. Phys. Chem. C* **2007**, *111* (40), 14925−14931.
(42) Tian, L. L.; Zhang, M. J.; Wu, C.; Wei, Y.; Zheng, J. X.; Lin, L. P.; Lu, J.; Amine, K.; Zhuang, Q. C.; Pan, F. γ-Fe_2O_3 nanocrystalline microspheres with hybrid behavior of battery-supercapacitor for superior lithium storage. *ACS Appl. Mater. Interfaces* **2015**, *7* (47), 26284−26290.
(43) Yin, L.; Gao, Y. J.; Jeon, I.; Yang, H.; Kim, J. P.; Jeong, S. Y.; Cho, C. R. Rice-panicle-like γ-Fe_2O_3@C nanofibers as high-rate anodes for superior lithium-ion batteries. *Chem. Eng. J.* **2019**, *356*, 60−68.

https://doi.org/10.1021/acsomega.4c11654
ACS Omega 2025, 10, 17673−17683